Geophys. J. Int. (2003) **153,** 317–332

Rock-magnetic properties of multicomponent natural remanent magnetization in alluvial red beds (NE Spain)

Pauline P. Kruiver, Cor G. Langereis, Mark J. Dekkers and Wout Krijgsman

Paleomagnetic Laboratory Fort Hoofddijk, Budapestlaan 17, 3584 *CD Utrecht, the Netherlands. E-mail: langer@geo.uu.nl*

Accepted 2002 September 24. Received 2002 August 15; in original form 2001 June 18

SUMMARY

An earlier study of the cyclic Miocene red bed sequence of La Gloria (Spain) by Krijgsman *et al.* indicated complicated behaviour of the natural remanent magnetization (NRM) in parts of the section, particularly close to reversal boundaries. We resampled part of the section with high resolution and used extensive rock-magnetic analyses to characterize the magnetic remanence carriers. Below a conspicuous hydromorphous layer, the magnetic contributions of haematite and magnetite are approximately equal, while in the brown layers on top of the hydromorphous layer the contribution of magnetite is drastically reduced. This is probably related to a change in hydrological conditions.

The NRM is characterized by: (1) a low-temperature (200–360 °C) overprint of unknown age, (2) a medium-temperature (360–580 °C) component, interpreted as the characteristic remanent magnetization (ChRM); and (3) a high-temperature haematite component (600–680 °C), carrying the same directions as the medium-temperature component. There is no perceivable delay in NRM acquisition between the medium- and the high-temperature components; they are both regarded as primary. The behaviour of the NRM seems to be similar in the cyclic lithologies. The acquisition of NRM thus seems to be independent of lithology in the cyclic part of the section. The higher sampling resolution yielded the detection of a new polarity zone, which probably represents a geomagnetic feature according to rock-magnetic properties. However, the more detailed magnetostratigraphy of the resampled part of the section indicates that the earlier correlation to the geomagnetic polarity timescale is no longer tenable. Therefore, the La Gloria section should no longer be used as a magnetostratigraphic dating tool of mammal biochronology.

Key words: isothermal remanent magnetization, magnetostratigraphy, Miocene, rock magnetism.

1 INTRODUCTION

Red beds form a vast amount of the geological record. However, the reliability of the natural remanent magnetization (NRM) in red beds for magnetostratigraphic purposes has often been questioned, because of the ambiguous origin of the magnetic carriers. Both the type and the timing of the remanence acquisition in red beds remain a subject of debate. Some argue that a chemical remanent magnetization (CRM) acquired long after deposition is the dominant mechanism, giving rise to a secondary NRM, while others suggest that haematite can carry a depositional remanent magnetization (DRM) and therefore a primary NRM. Even in the same red bed formation the origin of the magnetization remains controversial: for instance, Walker *et al.* (1981) and Larson *et al.* (1982) point out that the NRM in the Triassic Moenkopi Formation would be acquired over several tens of millions of years, whereas others argue that its NRM would be primary (Baag & Helsley 1974; Elston & Purucker 1979; Molina-Garza *et al.* 1991). In some other cases, a CRM and a DRM could be distinguished (Channell *et al.* 1982). Many studies have shown that haematite can indeed carry a reliable DRM signal (Tauxe *et al.* 1980; Steiner 1983; Tauxe & Badgley 1984; Krijgsman *et al.* 1999; Abdul Aziz *et al.* 2000; Kruiver *et al.* 2000). It is evident that a generalization of the reliability of all red beds cannot be made. In practice, this means that the reliability of each individual red bed sequence needs to be verified, using, for example, rock-magnetic methods.

The Teruel–Daroca–Calatayud Basin in NE Spain (Fig. 1) is a key area for developing a continental mammal biozonation in Western Europe. The area is rich in fossil sites, especially of Miocene age, and contains important climate information (Daams *et al.* 1999; van Dam *et al.* 2001). The Vallesian/Turolian boundary, represented by the mammal zone transition MN10/MN11 is dated magnetostratigraphically in the La Gloria section east of Teruel (Krijgsman *et al.* 1996). The section consists largely of red beds, and includes in specific intervals lacustrine limestones. The red beds display a clear cyclicity of red clays or silts and caliche beds. This

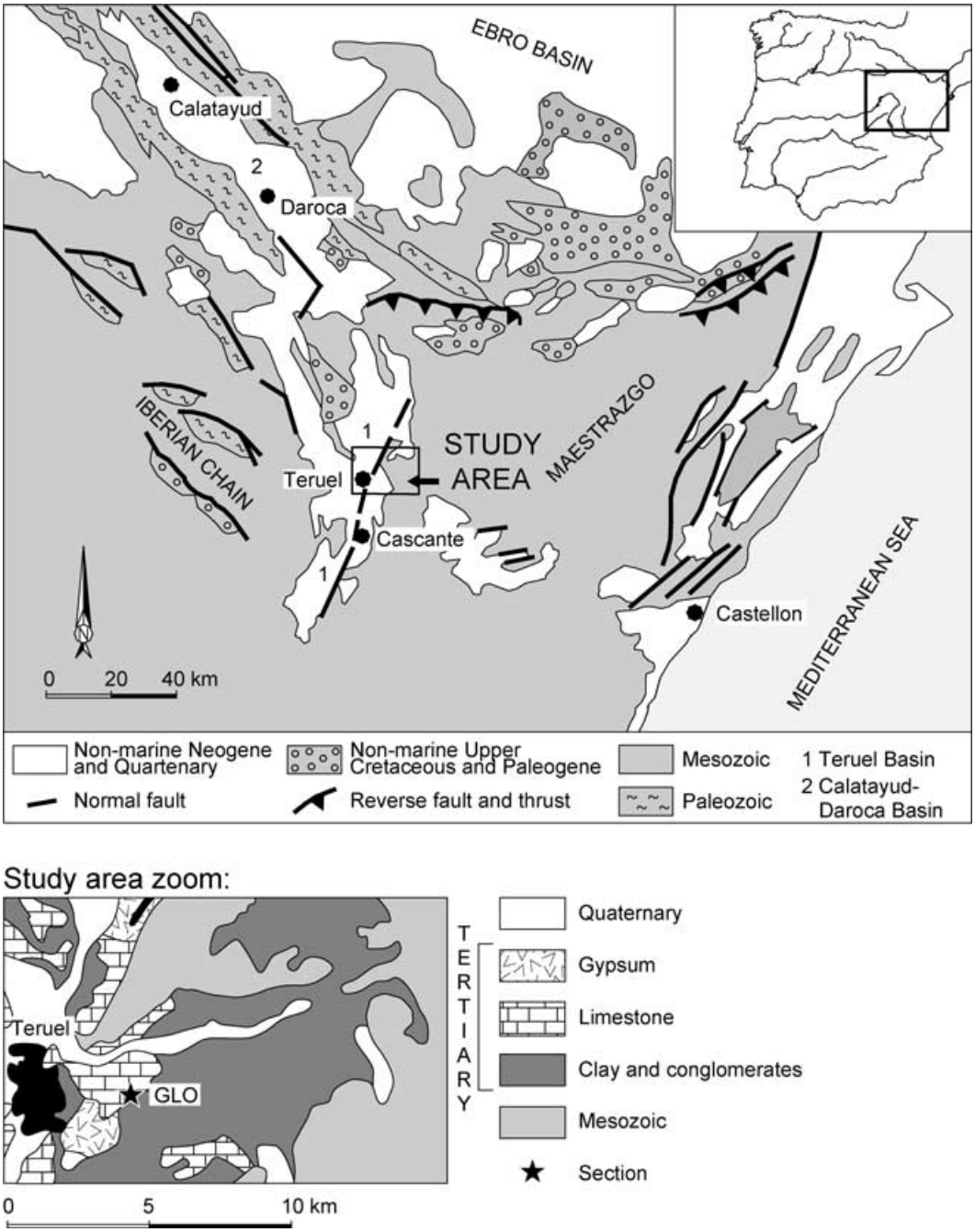

Figure 1. Location map of section GLO in NE Spain, east of the town of Teruel. The Neogene deposits of the study area are mostly bounded by Mesozoic formations.

cyclicity is probably related to climate. An earlier correlation of polarity zones of the La Gloria section to the GPTS seemed straightforward (Fig. 2). However, some intervals showed complex paleomagnetic behaviour with multiple NRM components, including a low-temperature reversed direction (Krijgsman *et al.* 1996). In other cyclic sediments the NRM behaviour was shown to be related to variations in lithology, and their accompanying processes of, for example, diagenesis (van Hoof *et al.* 1993; Krijgsman *et al.* 1997). Because in La Gloria the alternation of caliche beds and red clay beds is cyclic, the complex NRM behaviour might be linked to lithology as well, and therefore probably to climate. The presence of a reversed-polarity low-temperature component in the La Gloria section, and a possible lag between medium- and high-temperature components, requires further investigation. For this purpose, we have resampled in detail an interval of the La Gloria section containing several reversal boundaries.

2 GEOLOGICAL SETTING AND SAMPLING OF THE LA GLORIA SECTION

Thick alluvial and lacustrine Miocene sequences in Spain were deposited as a consequence of the tectonic evolution of the Iberian plate (Calvo *et al.* 1993, 1999). The Teruel–Daroca–Calatayud Basin in

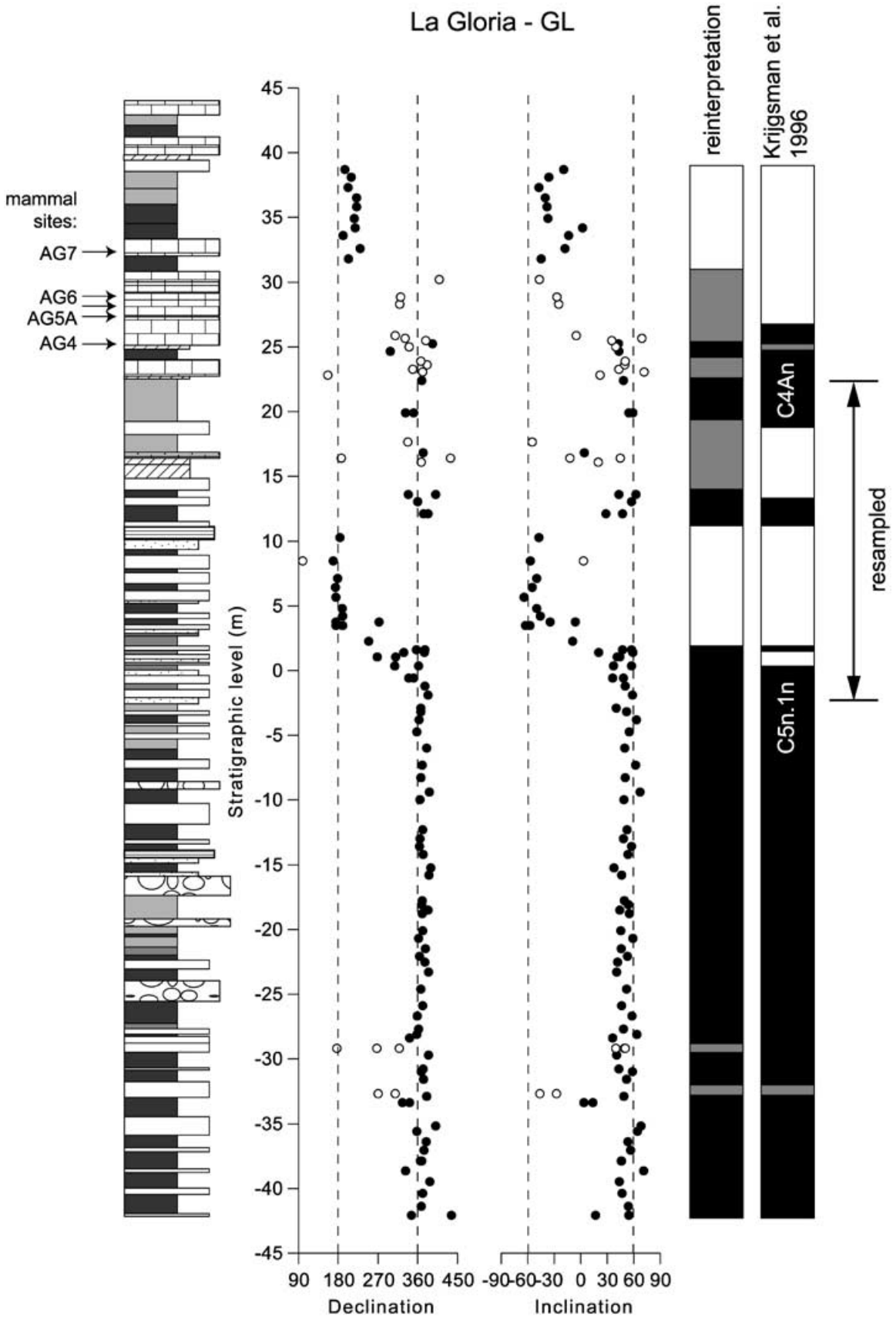

Figure 2. Original magnetostratigraphy and reinterpretation of the data. Data with high maximum angular deviation (MAD > 10) or no clear polarity are indicated by open circles. Lithological column: shaded, red clays; white, caliche; dotted, sandstone; diagonal hatch, yellow hydromorphous layer; horizontal hatch, cemented layer; bricks, limestone; boulders, conglomerates.

NE Spain appeared to be suitable for combined magnetostratigraphy and mammal stratigraphy (van der Meulen & Daams 1992; Daams *et al.* 1999; van Dam *et al.* 2001). In particular, the section of La Gloria in the Teruel Basin (∼90 m thick, Figs 1 and 2) has been used to construct a high-resolution magnetostratigraphy and biostratigraphy (Krijgsman *et al.* 1996; van Dam *et al.* 2001). The lower part of the section consists of a regular alternation of subhorizontal red silty clays or mudstones and intercalated caliche beds, with some sandy layers and conglomerates (Calvo *et al.* 1999). The clay mineral is predominantly illite, with smaller amounts of kaolinite. On top of the cyclic clay–caliche sequence there is a hydromorphous (bright yellow) layer and an interval of brown clays. Higher up the section evolves to a unit of biomicritic limestones. Several mammalian fossil sites are present in the limestone unit (indicated in the lithological column of La Gloria in Fig. 2), containing the MN zones 10 (J3) and 11 (K) (van Dam *et al.* 2001). On top of these limestones there are red mudstones again (Calvo *et al.* 1999).

The alternation of caliche beds and red clay layers in the lower part of the section is regular and cyclic, suggesting climatically forced variations in sedimentation. We define a basic small-scale sedimentary cycle as one caliche–red mudstone couplet. Typically, five small-scale cycles (∼1 m thick) form one large-scale cycle (∼6–7 m thick). Every fifth bed is thicker (∼2 m) and more pronounced in the field. This suggests that the small-scale cycles reflect the precession of the Earth's orbit (period of ∼22 kyr), while the large-scale cycles represent the eccentricity (period of ∼100 kyr). The cyclic sedimentation pattern is similar to the cyclicity observed in the Middle Miocene continental sections from the nearby Calatayud Basin (Fig. 1): the Armantes section (Krijgsman *et al.* 1997), the Orera section (Abdul Aziz *et al.* 2000) and the Cascante section in the Teruel Basin (Abdul Aziz 2001).

Earlier, Krijgsman *et al.* (1996) sampled one site per lithology, i.e. two sites for each caliche–red mudstone couplet, which resulted in a sampling resolution of approximately 80 cm for their series GL. For the present study, we resampled a 24 m thick stratigraphic interval containing the lower caliche–red mudstone sequence, which includes several reversal boundaries. We took samples at several levels in each lithology, resulting in an average sampling interval of 13 cm for the new series GLO.

3 METHODS

Stepwise thermal demagnetization has been applied to one or two samples from each stratigraphic level to determine characteristic remanent magnetization directions. Temperature steps of 40–50 °C were used up to 480 °C and steps of 20–30 °C up to 600 or 690 °C. The samples were heated and cooled in a laboratory-built, shielded furnace. The NRM was measured with a horizontal 2G Enterprises DC SQUID cryogenic magnetometer (with a noise level of 3×10^{-12} A m^2). To investigate the reliability and to determine the origin of the NRM signal, the directions of the NRM components were determined with principal-component analysis (Kirschvink 1980) using at least four temperature steps for each component.

Thermomagnetic runs were performed for 10 powdered samples from different lithologies in air up to 700 °C on a modified horizontal translation-type Curie balance (with a noise level of 5×10^{-9} A m^2) (Mullender *et al.* 1993). The magnetic susceptibility versus temperature was measured for seven powdered samples up to 700 °C with a CS3 furnace attached to a KLY3 susceptibility bridge (AGICO, Brno, with a noise level of 3×10^{-8} SI for a standard 10 cm^3 sample at room temperature). The KLY3/CS3-experiment was performed in a N_2 atmosphere to limit oxidation of the samples during heating. Each sample was flushed with N_2 before initiation of the experiment. Also, partial runs of magnetic susceptibility up to 200, 400, 600 and 700 °C were measured in air for two samples on the KLY3/CS3.

Hysteresis loops were measured for 19 samples from all lithologies with an alternating gradient magnetometer (MicroMag Model 2900, Princeton, with a noise level of 2×10^{-10} A m^2) to determine the saturation magnetization (M_s), the saturation remanence (M_r) and the coercive force (B_c). Because of partial saturation of the pole shoes, the response of the MicroMag is not linear for fields above 1.6 T. Therefore, we applied maximum fields of 1.6 T in all cases. The averaging time for each measurement was 0.1 s with field increments of 8 mT. Backfield curves allowed determination of the coercivity of remanence (B_{cr}) after application of a 1.6 T positive field.

To assess the magnetic domain state, the effects of magnetic interactions and magnetic mineralogy, first-order reversal curves (FORC) (Pike *et al.* 1999; Roberts *et al.* 2000) were measured for three representative samples from different lithologies. To determine a FORC diagram, one proceeds as follows. First, a large positive field is applied and ramped down to the reversal field B_a. Then, the magnetization is measured as the field B_b is increased from B_a back up to saturation. A mixed second derivative of the magnetization with respect to B_a and B_b defines the FORC distribution, which is displayed as a contour plot. It is convenient to apply a change of coordinates to B_u ($\equiv (B_a + B_b)/2$) and B_c ($\equiv (B_b - B_a)/2$). In this way, B_c may be interpreted as particle coercivity and B_u as the local interaction field. A smoothing factor (SF) is applied to suppress noise in the contours of the FORC diagram. The contour patterns in a FORC diagram are distinctly different for superparamagnetic, (pseudo)single-domain or multidomain behaviour, whereas deviations from the $B_u = 0$ axes indicate magnetic interactions (Pike *et al.* 1999; Pike *et al.* 2001; Roberts *et al.* 2000).

For each FORC diagram, 200 curves were measured with an averaging time of 0.2 s per data point. We measured during the night to minimize noise. Again, the maximum applied fields were 1.6 T. Two runs were performed for each sample: (1) measurements were focused on the low-coercivity range: B_c ranges between 0 and 50 mT and $-50 \leq B_u \leq 50$ mT and (2) measurements were focused on the higher coercivity range: measured B_c ranges between 0 and 600 mT (displayed as 60–600 mT) and $-50 \leq B_u \leq 50$ mT.

Acquisition curves of isothermal remanent magnetization (IRM) were determined for 99 stratigraphic levels, using 28–30 acquisition steps with fields up to 2.5 T. The peak fields were applied with a PM4 pulse magnetizer and the IRM intensity measured either on a JR5A spinner magnetometer (AGICO, Brno, with a noise level of 10^{-11} A m^2) or on the 2G Enterprises DC cryogenic magnetometer, depending on the physical state of the samples. The IRM acquisition curves were decomposed into magnetic components using the IRM fitting program of Kruiver *et al.* (2001). The IRM acquisition curves are cumulative log-normal with respect to the pulse field. Components add linearly in the acquisition curve, provided no magnetic interactions occur. Each magnetic component can be characterized by: (1) its saturation IRM (SIRM); (2) the peak field at which half of the SIRM is reached ($B_{1/2}$); and (3) the dispersion of the cumulative log-normal distribution (DP). The residuals between the measured data and fitted curves are interactively minimized by adjusting the IRM component parameters.

4 INVESTIGATION OF MAGNETIC REMANENCE CARRIERS

4.1 NRM behaviour

Representative thermal demagnetization diagrams of the resampled section are shown in Fig. 3. Up to four components can be detected in the thermal demagnetization plots: (1) a present-day field or laboratory overprint up to 200 °C; (2) a low-temperature (LT) component ranging from 200 to 360 °C; (3) a medium-temperature (MT) component ranging from 360 to 570/580 °C residing in magnetite; and (4) a high-temperature (HT) component ranging from 600 up to 680/690 °C residing in haematite. In the demagnetization plots, the MT and HT components have the same polarity. There is no perceivable delay in NRM acquisition between the MT and HT as was observed at Armantes, for example, (Krijgsman *et al.* 1997). Magnetite and haematite have a different mechanism of formation: the magnetite is most probably detrital and the haematite might be detrital or is probably present as a coating. The observation that these two minerals display the same polarity behaviour indicates a primary origin for these NRM components.

Although goethite seems to be present in the entire section (see Section 4.3), it is present in only minor amounts (except for the hydromorphous layer) and hardly contributes to the NRM.

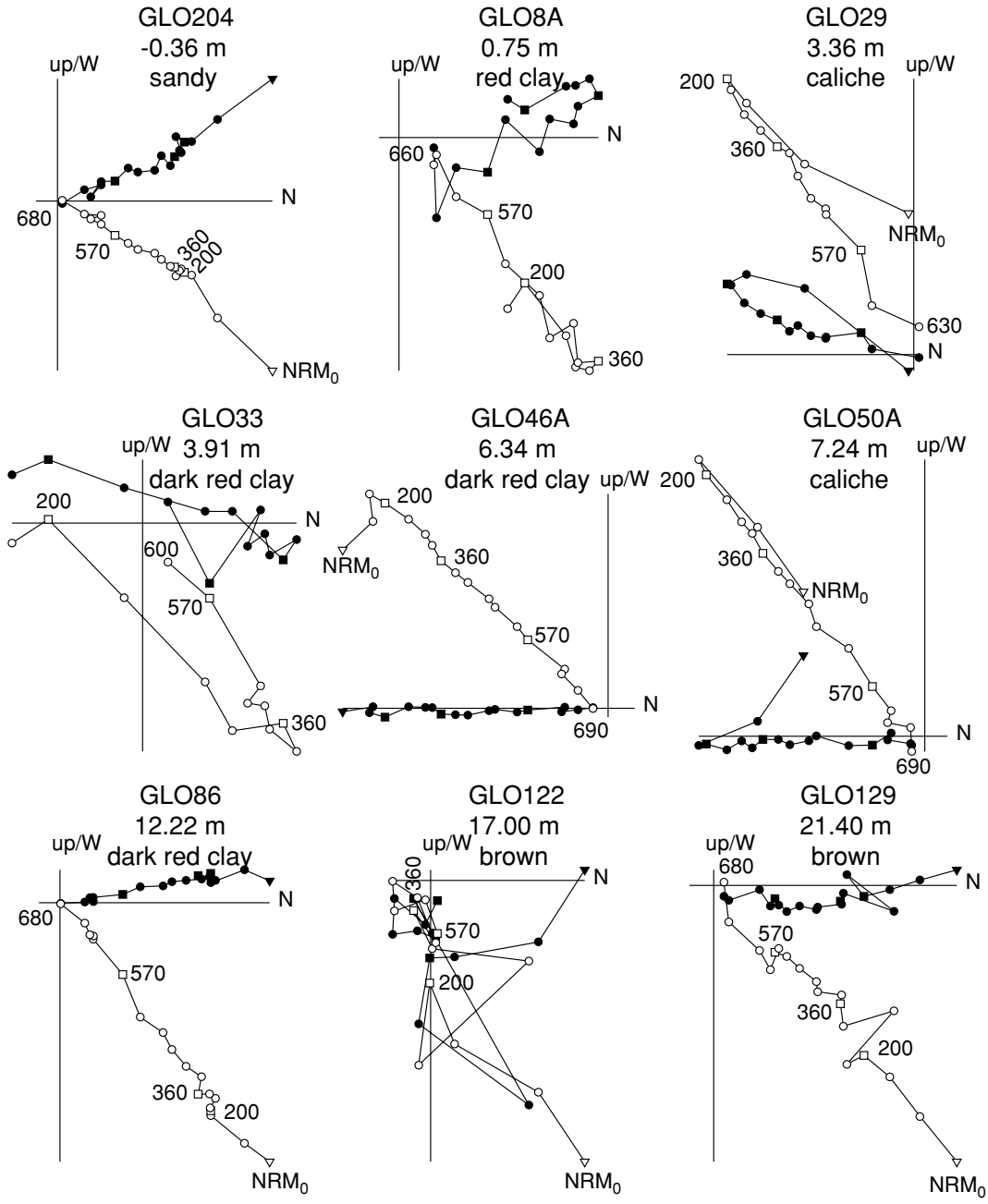

Figure 3. Characteristic thermal demagnetization diagrams through the section. Open (solid) symbols indicate projection on the vertical (horizontal) plane. The stratigraphic level and lithology are indicated below the sample code. The triangle represents the initial NRM; other relevant temperature steps (200, 360 and 570 °C) are indicated by squares.

Moreover, the maximum unblocking temperature of goethite is 120 °C (e.g. Dekkers 1998), so it does not interfere with the magnetite or haematite directions. In the hydromorphous layer, goethite does not appear to carry a stable NRM direction.

The LT component behaviour is remarkable (Fig. 3): for normal polarity MT and HT components, the LT component is either reversed (e.g. GLO8A and GLO33), or it shows hardly any decay (GLO129) or forms a cluster (GLO204 and GLO86). For reversed-polarity MT and HT components, the LT component is always reversed and decays progressively (GLO29, GLO46A and GLO50A). This must mean that the blocking temperature spectrum of the LT component partially overlaps with that of the MT magnetite component. It is either stronger (GLO8A, GLO33) or weaker (GLO129) than the magnetite component that unblocks up to 570–580 °C. This kind of behaviour, with a clustered low-temperature component, is observed in other continental sections as well (e.g. Abdul Aziz *et al.* 2000). In Section 5.1, LT and MT components are simulated to explain the observed directional behaviour in the thermal demagnetization diagrams.

4.2 Thermomagnetic runs

To understand the different NRM components and to determine which of these are primary or secondary, we carried out several rock-magnetic measurements. In thermomagnetic runs (Fig. 4), the total magnetization of all samples (left-hand panels) is dominated by a paramagnetic contribution, indicated by the hyperbolic form of the curves. The small change in slope at ∼670 °C that is reversible on cooling is indicative of the Néel temperature of haematite. The heating and cooling curves diverge at ∼600 °C, owing to thermal alteration above 600 °C. A very slight change of slope at ∼600 °C indicates a magnetite contribution. The detectable Néel temperature of haematite implies that there is an appreciable concentration of haematite (by weight) in the sample, given the large difference in saturation magnetization at room temperature between magnetite (90–92 A m^2 kg^{-1}) and haematite (0.4 A m^2 kg^{-1}) (Hunt *et al.* 1995). The only sample for which a clear change in slope is detectable near 350 °C—at the transition temperature of the LT and MT components—is GLO13A (Fig. 4b).

The temperature-dependent behaviour of magnetic susceptibility is more sensitive to magnetite than to haematite. When measured in air, all curves were reversible up to 600 °C (not shown). After heating to 700 °C the cooling curve dropped slightly below the heating curve (Fig. 4, central panels). The drop in susceptibility between 550 and 600 °C is indicative of magnetite. However, magnetite becomes oxidized to form maghaemite upon heating in air, resulting in a slightly higher Curie temperature when compared with the N_2 runs (Fig. 4, right-hand panels). When the heating and cooling are performed in an N_2 atmosphere, both in the heating and the cooling curve two segments appear to be present within the magnetite range, which we presume is related to the observed LT and MT components in the NRM.

4.3 Hysteresis loops and FORC diagrams

All measured hysteresis loops are wasp-waisted (three examples are shown in Fig. 5), as is typical for mixtures of low- and high-coercivity materials (Roberts *et al.* 1995; Tauxe *et al.* 1996). We selected three samples for the measurement of FORC diagrams (Fig. 6). The low-coercivity range FORC diagrams for samples

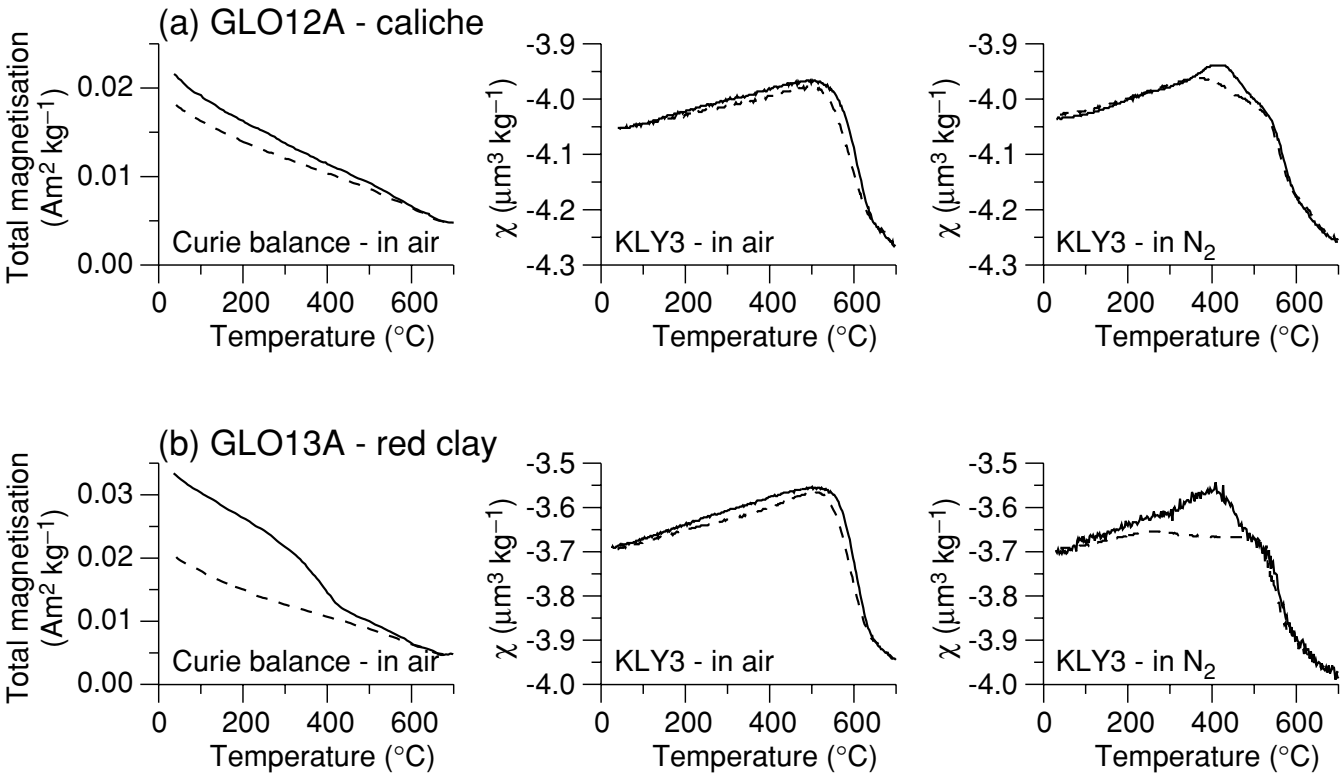

Figure 4. Representative thermomagnetic runs for sample (a) GLO12A and (b) GLO13A. From left to right, measured with: Curie balance in air; KLY3/CS3 susceptibility bridge in air; KLY3/CS3 susceptibility bridge in N_2 (continued flushing). Solid (dashed) lines indicate heating (cooling) curves. No furnace tube correction was applied for the KLY 3 experiment, resulting in negative values for the magnetic susceptibility.

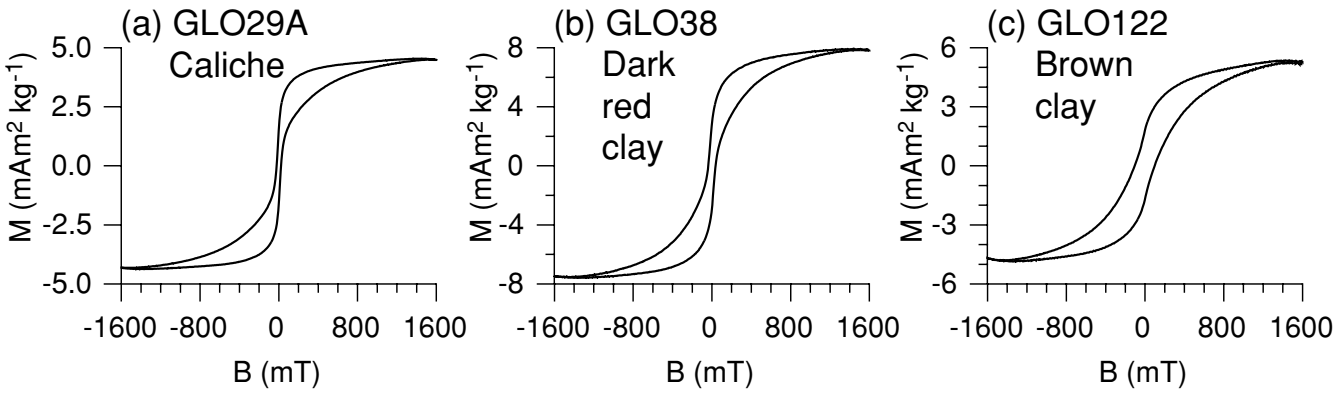

Sample	B_c	B_{cr}	B_{cr}/B_c	M_r	M_s	M_r/M_s
GLO29A	22.8	164	7.2	1.61	4.40	0.37
GLO38	37.5	187	5.0	2.84	7.67	0.37
GLO122	101	350	3.5	1.75	5.00	0.35

Figure 5. Representative hysteresis curves from samples: (a) GLO29A, stratigraphic level 3.41 m, (b) GLO38, 4.92 m, (c) GLO122, 17.00 m. B_c and B_{cr} in mT; M_r and M_s in mA m^2 kg^{-1}.

GLO29A (caliche) and GLO38 (red clay) look similar: there is a narrow peak with respect to B_u, which is centred around $B_u = 0$, indicating negligible magnetic interactions. There is a larger spread along the B_c-axis than along the B_u-axis. The peak occurs at ∼15–20 mT. The contours are closed on the left-hand side of the FORC diagram, which is indicative of SD behaviour (Pike *et al.* 1999; Roberts *et al.* 2000). The FORC diagrams of the high-coercivity range show a band of contours up to 600 mT. This indicates a high-coercivity mineral in addition to the SD magnetite: this mineral is most probably haematite and/or goethite.

The low-coercivity run of sample GLO122 (brown clay) was too noisy for meaningful interpretation, because the magnetite signal in this lithology is low (see Section 4.4). Consequently, the haematite/goethite contribution in the high-coercivity range is clearer (Fig. 6e). As inferred from IRM component analyses of many samples (Section 4.4), the band of contours up to 350 mT represents haematite, while the high-coercivity contours up to 600 mT indicate goethite. Although the red colour and the IRM acquisition curves do not suggest the presence of goethite (except in the yellow hydromorphous layer), it is probably present in minor amounts throughout the entire section (van Oorschot *et al.* 2001).

4.4 IRM component analysis

FORC diagrams (Fig. 6) indicate that magnetic interactions are negligible in the La Gloria samples, which makes IRM component analysis applicable. Representative examples of IRM analyses from the bottom part of the section, from the hydromorphous layer and from a brown clay layer are given in Fig. 7. The magnetic components can be characterized by their SIRM, $B_{1/2}$ and DP values (Fig. 8). All samples contain (at least) two magnetic components: either magnetite and goethite in the hydromorphous layer or (lower coercivity) magnetite and haematite in the remainder of the section. No distinction can be made between goethite and haematite (apart from two samples at ∼14.5 m), because of their coercivity overlap, and the limited number of data points in the high-field range. In the hydromorphous layer, the bright yellow colour points to goethite, whereas the red colour in the remainder of the section indicates the presence of haematite. Therefore, it is conceivable that the second IRM component represents goethite in the hydromorphous layer, whereas it represents haematite (perhaps with a small goethite contribution) elsewhere.

The SIRM of the magnetite component (component 1) correlates with lithology in the lower part of the section (Figs 8a and b). Generally, it is lower in the caliches than in the red clays. $SIRM_{magnetite}$ is lower at 14 m and above. The change in magnetic properties at 14 m is also obvious in the mean coercivities of the magnetite component (Fig. 8d): below 14 m, the mean coercivity is rather constant (average $B_{1/2} = 25$ mT), with a low dispersion (average DP = 0.32; units of DP are log $_{10}$(mT)). In the hydromorphous layer, the magnetite has a higher mean coercivity (65 mT) and has a much higher DP (0.48). The higher DP indicates that the magnetite is more oxidized in this interval. Above the hydromorphous layer, the coercivity of the magnetite is higher and more variable (average 42 mT) than below 14 m, with DPs similar to those in the hydromorphous layer (0.43). Therefore, the magnetite in and above the hydromorphous layer is inferred to be more oxidized compared with below.

The SIRM pattern of the haematite component (component 2) displays a different pattern compared with $SIRM_{magnetite}$ (Fig. 8c). The variability of $SIRM_{haematite}$ is of the same order of magnitude in the lower part and in the upper part of the section, except for the hydromorphous layer. The lower $SIRM_{haematite}$ values seem to predominate in the caliche layers, as is the case for $SIRM_{magnetite}$. The $SIRM_{haematite}$ is somewhat elevated between 4 and 14 m, with a drop in the sandy interval between 9 and 12 m. As is the case for the SIRM, fluctuations of mean coercivities of the magnetite component are not mirrored by the haematite component (Fig. 8e). The coercivity of the haematite varies between ∼450 and 650 mT (with an average of $B_{1/2} = 530$ mT) with an average DP of 0.40. The hydromorphous layer clearly departs from this trend: the second component has a much higher coercivity (2.0 T), with generally lower DP (0.31), and represents goethite. In a small interval (14.4–14.6 m), the goethite and haematite contributions can be separated. In these samples, a three-component fit was significantly better at the

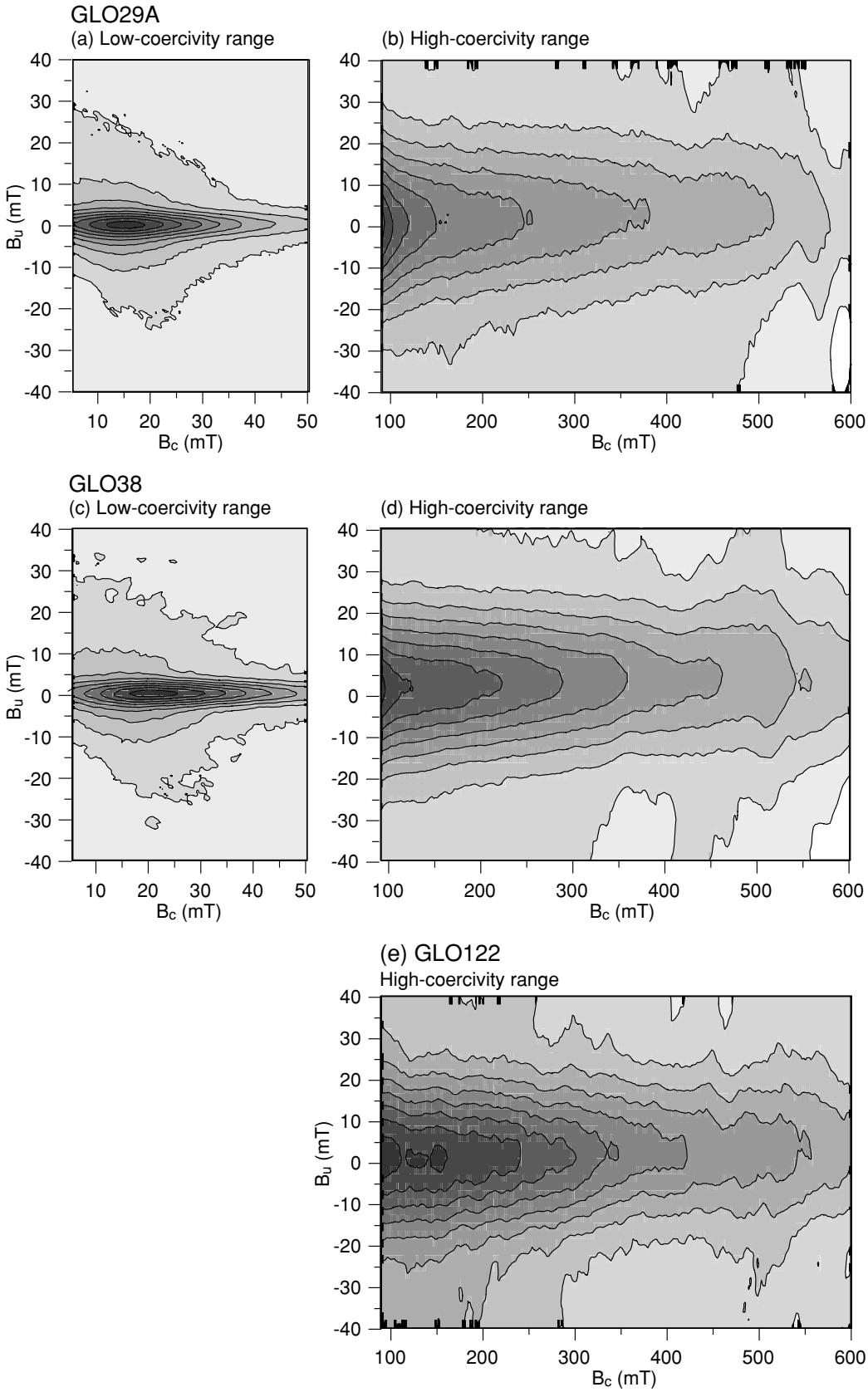

Figure 6. FORC diagrams for three samples. (a) GLO29A, caliche; (b) GLO38, red clay; (c) GLO122, brown clay. Each panel shows 10 contours and is normalized to its maximum value. Dark (light) represents high (low) values. Left-hand panels focus on the magnetite coercivity range (SF = 6 with 200 curves) and right-hand panels on the haematite coercivity range (SF = 8 with 200 curves). The magnetite range FORC diagram for GLO122 was very noisy and is therefore not shown.

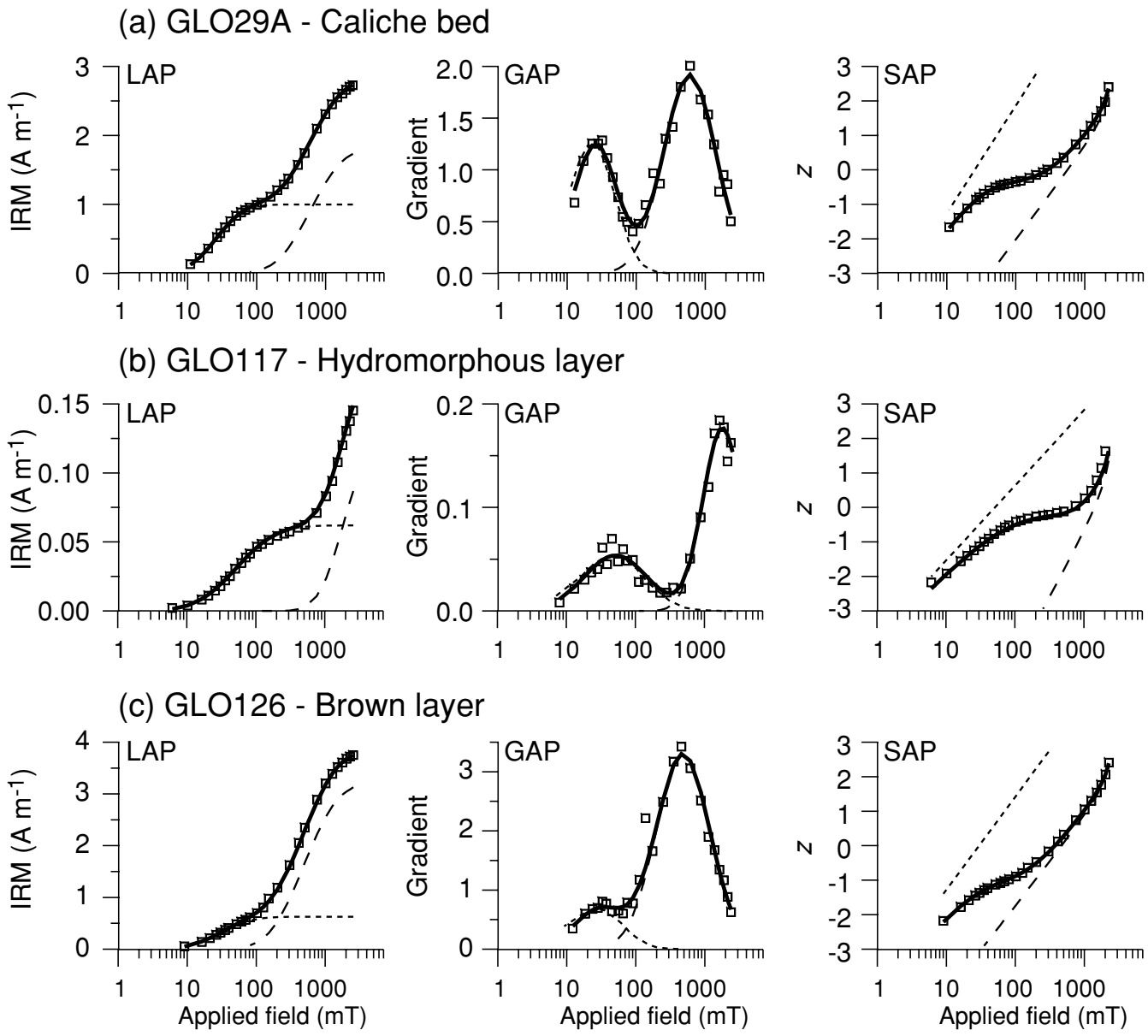

	Component 1				Component 2			
	SIRM	$^{10}\log(B_{1/2})$	± DP	$B_{1/2}$	SIRM	$^{10}\log(B_{1/2})$	± DP	$B_{1/2}$
GLO29A	1.00	1.41	0.32	25.7 mT	1.83	2.78	0.38	0.603 T
GLO117	0.0637	1.74	0.48	55.0 mT	0.106	3.22	0.23	1.66 T
GLO126	0.629	1.47	0.37	29.5 mT	3.23	2.68	0.39	0.479 T

Figure 7. Representative examples of the IRM component analysis. Squares are data points, the thin short (long) dash represents the best fit of component 1 (2), the solid line is the best-fitting sum of components. Component 1 consists of magnetite and component 2 of haematite, possibly with a goethite contribution. (a) Linear acquisition plot (LAP), gradient acquisition plot (GAP) and standardized acquisition plot (SAP) for sample GLO29A from the bottom part of the section, stratigraphic level 3.41 m. (b) LAP, GAP and SAP for sample GLO117 from the bright yellow hydromorphous layer (16.09 m), with goethite dominance instead of haematite. (c) LAP, GAP and SAP for sample GLO126 from the brown clay layer between the hydromorphous layer and the limestones, 19.60 m. SIRM in A m^{-1}; $\log_{10}(B_{1/2})$ and DP in $\log_{10}$(mT).

95 per cent confidence level than a two-component fit. The goethites in this interval have mean coercivities of 1.5 and 1.8 T with a DP of 0.44 and 0.45 ($\log_{10}$ mT), respectively, which is comparable to that in the hydromorphous layer. The haematites have mean coercivities of 215 and 270 mT (DP = 0.31 and 0.36), which is lower than in the remainder of the section. This could be caused by a minor goethite contribution elsewhere in the section, where haematite and a possible goethite contribution could not be separated.

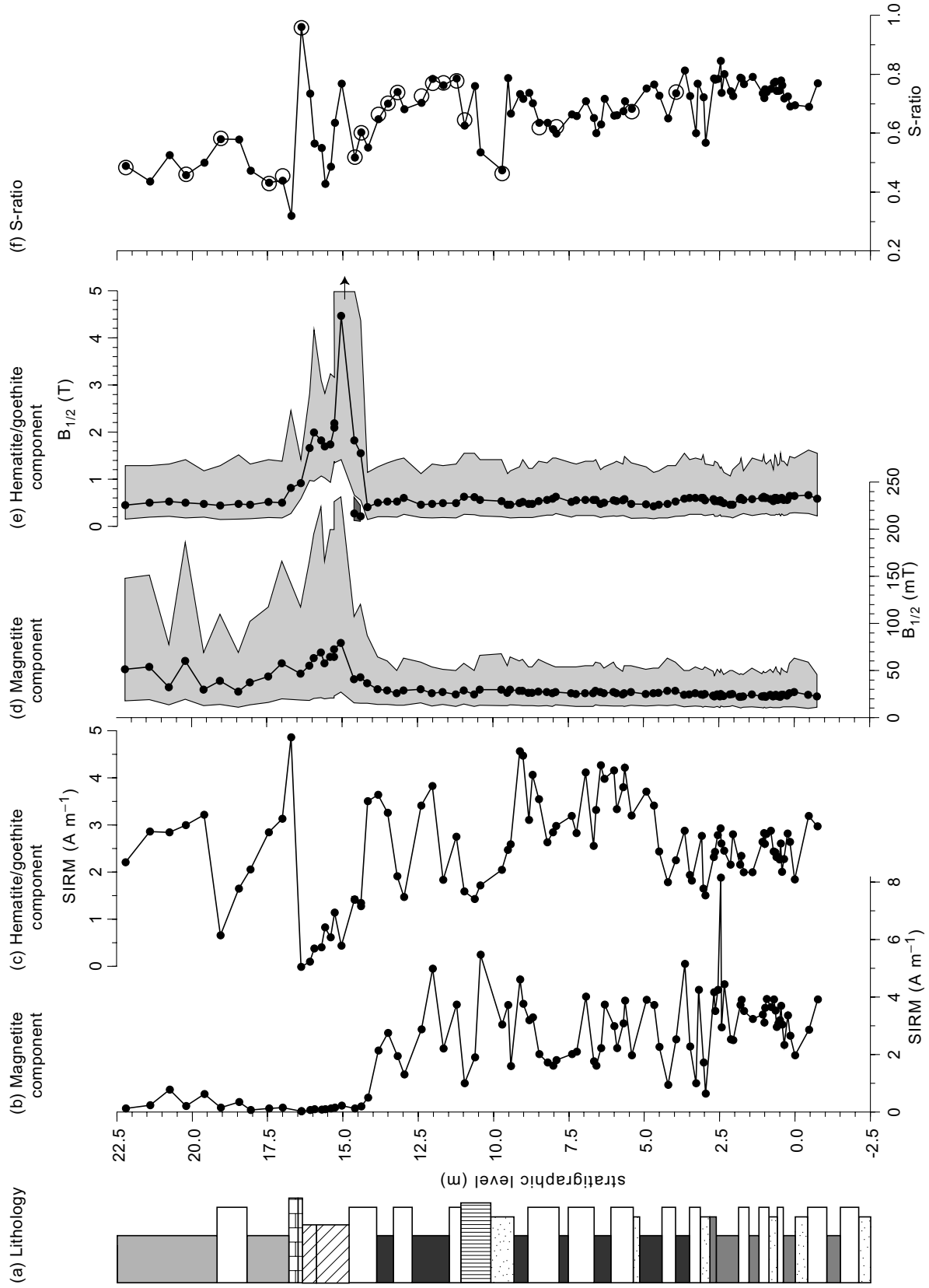

Figure 8. Magnetic properties as inferred from the IRM component analysis versus stratigraphic level. (a) Lithological column as in Fig. 2. (b) SIRM of the magnetite component. (c) SIRM of the haematite and the goethite component. (d) $B_{1/2}$ of the magnetite component. (e) $B_{1/2}$ of the haematite and the goethite component. The interval of 14.4–14.6 m contains separable haematite and goethite components. Shaded areas denote $B_{1/2}$ ± the antilog of DP. (f) *S*-ratio (1-IRM$_{-0.3T}$/IRM$_{1T}$)/2 (Bloemendal *et al.* 1992), which anticorrelates with SIRM$_{haematite}$/SIRM$_{magnetite}$. Open circles denote measured *S*-ratios and closed symbols are calculated S'-ratios from the modelled IRM components (Kruiver & Passier 2001).

The *S*-ratio (Fig. 8f), both measured and calculated (S') from the IRM components (Kruiver *et al.* 2001), shows good anticorrelation with $SIRM_{haematite}/SIRM_{magnetite}$. Therefore, it can be interpreted as a proxy for the relative contributions of low- versus high-coercivity material: lower values of the *S*-ratio indicate a higher relative contribution of the high-coercivity material (haematite and/or goethite).

5 DISCUSSION

5.1 Simulation of NRM components

The NRM shows three distinctive components: a LT component, carried by part of the magnetite assemblage; an MT component, which partly overlaps with the LT component and is carried by the remaining part of the magnetite assemblage; and a HT component, carried by haematite. The distinction between magnetite and haematite is apparent from all measurements: in the thermal demagnetization diagrams, as wasp-waisted hysteresis loops, as two distinctive IRM components and as a magnetite peak and haematite band in the FORC diagrams. Although the rock-magnetic techniques could not discriminate between the two fractions of 'magnetite' (except for the KLY3 measurements in N_2), they are evident from their principally different NRM directions. The apparent unblocking temperature of ~360 °C of the LT component could indicate that part of the magnetite assemblage has been oxidized to cation-deficient magnetite or even to maghaemite, depending on the degree of oxidation. We use the term 'magnetite' to refer to these possibilities for both the LT and MT components. It appears that the two fractions of the magnetite assemblage compete with each other: as a rule, the LT component has a reversed polarity, while the MT component displays both polarities. These components seem to be present throughout the section from the bottom up to the hydromorphous layer. The LT component is not only present in the part of the La Gloria section that we resampled in detail, but also in the originally sampled series GL. In the original study, the stationary 200–360 °C component seems to predominate in the red mudstones. In our more detailed sampling, however, there seemed to be no correlation between the appearance of the LT component and the lithology.

We simulated thermal decay curves of two directionally nearly opposite magnetic assemblages with different unblocking temperatures. A haematite contribution was not included, because the HT component showed the same directions as the MT component. Moreover, the haematite component will not overlap in unblocking spectrum with the LT component. We varied the relative intensities of the LT and MT components to investigate the directional behaviour observed in the thermal demagnetization diagrams. Similar to the exponential behaviour of the relaxation time with temperature for SD grains (Néel 1955), we approximated thermal decay curves by

$$\text{intensity}(T) = 1 - \exp\left(\frac{T - T_{\text{unblock}}}{T_{\text{unblock}} - T_{\text{start}}}\right), \quad (1)$$

where T is the temperature in °C, and the simulated thermal component unblocks between T_{start} and T_{unblock}. The first magnetite component represents the LT component and is modelled by $T_{\text{start}} =$

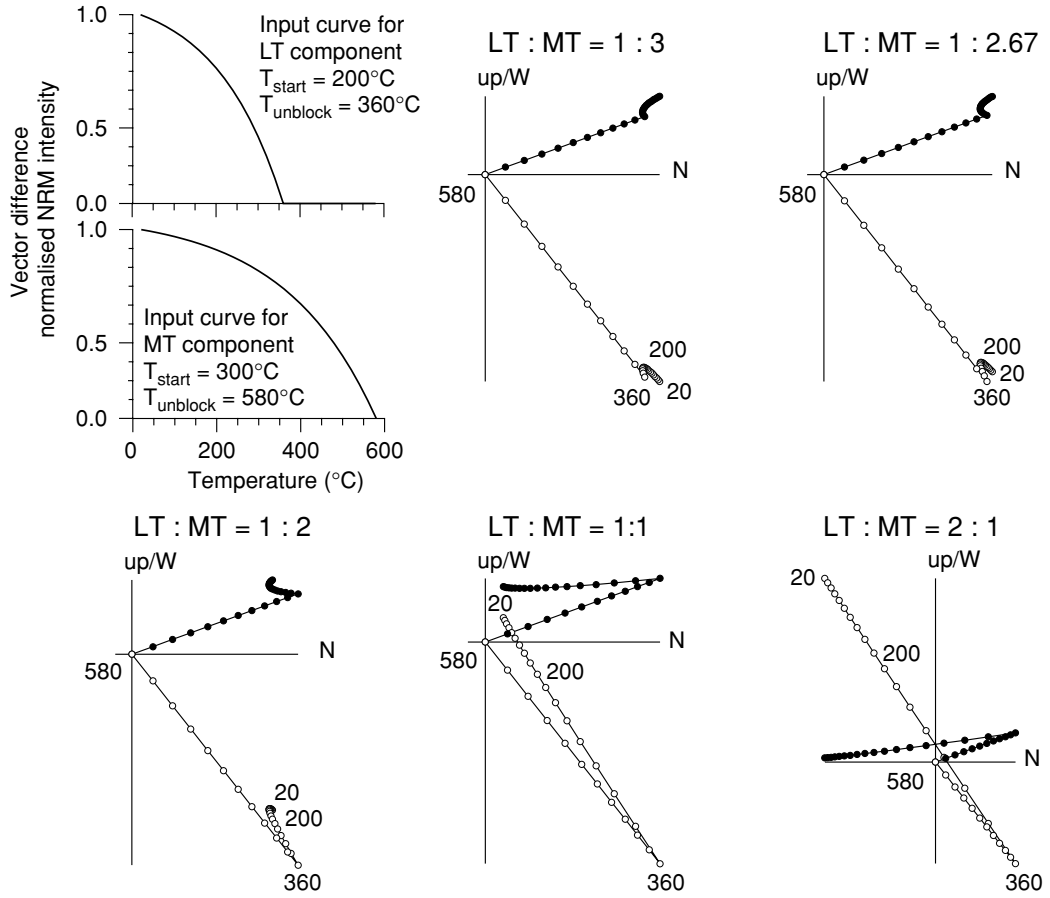

Figure 9. Simulated thermal demagnetization diagrams. Input decay curves are simulated using eq. (1) for the LT and MT component in the upper left-hand corner. LT and MT components are added by vector addition with relative intensities LT:MT ranging from 1:3 to 2:1 for the thermal demagnetization diagrams. Symbols are shown at 20 °C intervals and open (solid) symbols indicate projection on the vertical (horizontal) plane.

200 °C and $T_{unblock}$ = 360 °C. The second magnetite component (representing the MT component) is modelled with a partly overlapping unblocking trajectory of T_{start} = 300 °C and $T_{unblock}$ = 580 °C (Fig. 9). In our model, the LT component was given reversed polarity (declination = 170°; inclination= −55°) and the MT component was assigned a normal polarity direction (declination=340°; inclination=50°). Their directions are chosen to be not perfectly antipodal, because in this way their behaviour is better visualized in the simulated thermal demagnetization diagrams. The intensities of the LT and MT components were normalized to the intensities at 20 °C. We combined the LT and MT components in various relative intensities ranging from LT:MT = 1:4 to 4:1 (Fig. 9, shown from 1:3 to 2:1) by vector addition. When the LT component is small relative to the MT component (1:4 and 1:3), there is hardly any decay between 200 and 360 °C. The thermal demagnetization diagram of GLO204 (Fig. 3) corresponds to this kind of behaviour. For 1:2.67, the trajectory between 200 and 360 °C shows a curl, which is observed in sample GLO86 (Fig. 3). From 1:2 onwards, the typical zigzag thermal demagnetization diagrams emerge. The thermal demagnetization diagram of GLO8A (Fig. 3) is similar to 1:2, whereas GLO33 (Fig. 3) displays an even larger LT component (1:1 to 2:1). More extreme cases are not observed for the GLO samples.

Thermal decay data of GLO samples are shown in Fig. 10, together with the simulated curves. Data from temperature steps between 20 and 200 °C have been omitted, because of a laboratory or present-day field contribution. Also, the haematite contribution was not modelled and has been removed from the decay data. For clarity, the curves in Fig. 10 are normalized using the intensity value at 240 °C. Although there is a large spread among the data points, both for the cluster 200–360 °C and the zigzag plot, the GLO decay data clearly follow the simulated decay curves. We determined the GLO thermal decay data using vector differences from occasionally noisy demagnetization diagrams. Therefore, some curves display an apparent decrease in intensity with increasing temperature, whereas in fact they are stationary. This is why sample GLO86 plots above sample GLO204, even though they show similar behaviour in the thermal demagnetization diagram. For samples GLO8A and GLO33, however, the decay curves plot where they are expected: GLO33, which has a relatively large LT component plots between the 1:1 and 2:1 model curves; GLO8A, which has a smaller LT component plots in the vicinity of the 1:2 model curve.

The directional behaviour in the thermal demagnetization diagrams can be explained using the simplified model for thermal decay of two competing components. Depending on the relative intensity of the reversed-polarity LT component and the normal polarity MT component, the LT component either has a clearly reversed-polarity trajectory (zigzag thermal demagnetization diagram) or seems to show no or very little decay (cluster) between 200 and 360 °C. This agrees with the assumption that there is only one magnetite carrier (as suggested by the IRM analysis), of which only part is remagnetized during a period of reversed polarity.

From the identical MT and HT directions and the fact that the LT component is essentially reversed, we conclude that the MT and HT polarity zones represent the primary geomagnetic polarity and that the reversed-polarity LT component is a later overprint. The actual process that caused the reversed-polarity overprint is unclear. We speculate that it is related to the change in environment above 14 m and the subsequent change to lacustrine limestones.

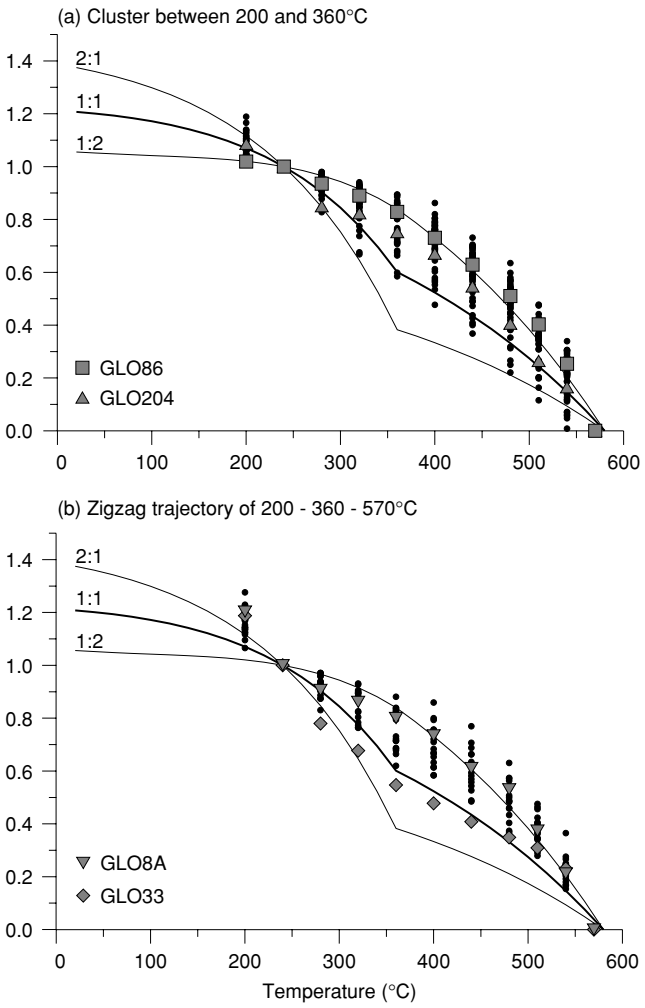

Figure 10. Simulated thermal decay curves (lines) and GLO thermal decay data (dots). (a) GLO data with clustered thermal demagnetization diagrams between 200 and 360 °C. GLO86 and GLO204 (Fig. 2) are represented by the squares and triangles, respectively. (b) GLO data with zigzag thermal demagnetization diagrams. GLO8A and GLO33 (Fig. 2) are represented by inverted triangles and diamonds, respectively.

5.2 Environmental implications

In the La Gloria section, there is a change in sedimentary environment at 14 m: the cyclic lower part of the section gives way to a hydromorphous layer, with brown clays above, which terminate in lacustrine limestone beds. This break at 14 m is reflected in the IRM component analysis (Fig. 8): for the magnetite component, SIRM values decrease by an order of magnitude, and the mean coercivities and DP values increase. This indicates that the magnetites become more oxidized, and occur in much lower concentrations. The haematite IRM component, however, does not follow this pattern.

The IRM variations throughout the section can be visualized by plotting SIRM, $\log_{10}(B_{1/2})$ and DP as a 3-D plot (Fig. 11). For the magnetite component (Fig. 11a), we observe a cloud of data points of variable (medium to high) SIRM and low $\log_{10}(B_{1/2})$; magnetite-bearing samples are red clays, sandy layers and caliches. The hydromorphous layer plots in the upper left-hand corner, with high $\log_{10}(B_{1/2})$ and DP and relatively low SIRM values. Samples from the brown layers (and some caliche samples stratigraphically close to the brown layers) plot in the region between the hydromorphous layer and the caliche/red clay data cloud. These

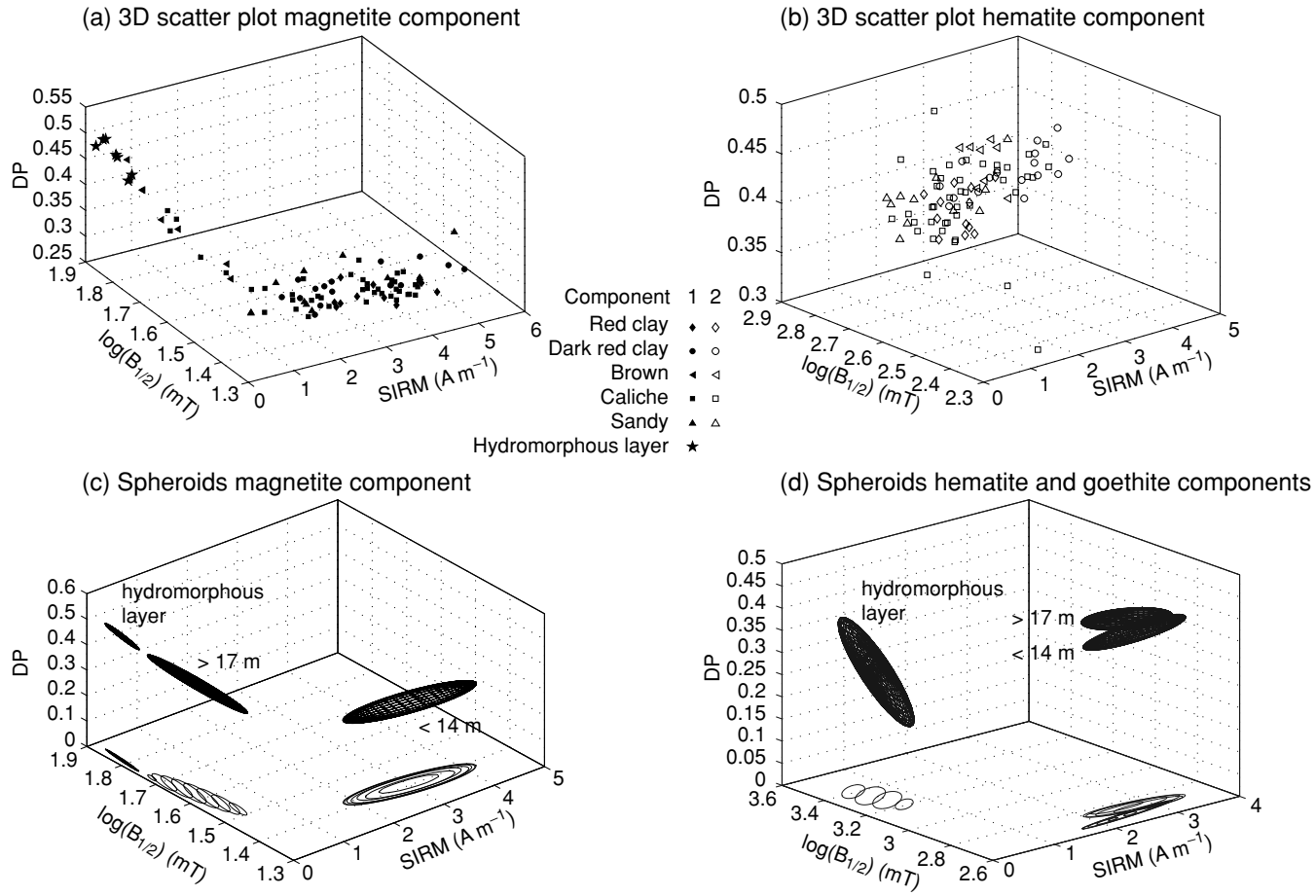

Figure 11. 3-D representation of the IRM component analysis parameters for each lithology. (a) Component 1 and (b) component 2; the hydromorphous layer is not shown, because it plots beyond the reach of the 3-D axes. See the legend for symbols. 3-D spheroid representation with projection of the lower plane of the lower (<14 m) and the upper (>17 m) part of the section and the hydromorphous layer for (c) component 1 and (d) component 2.

brown samples appear to have intermediate properties between the caliche/red clay samples and the altered hydromorphous layer. The picture is different for the haematite component. In the scatter plot (Fig. 11b), the brown samples cannot be distinguished from the caliche–red clays.

The 3-D analysis of IRM parameters indicates that a distinction based on general sedimentary intervals (red sediments below 14 m, and brownish sediments above 17 m, with the extreme of a hydromorphous layer in between) makes more sense than a distinction based on caliche/clay lithology. We have plotted the standard deviations in the principal-component directions (eigenvectors) as spheroids for the interval of <14 m, for the hydromorphous layer and for the interval of >17 m (Figs 11c and d). From this representation of the IRM data, it is even more clear that the magnetite component in the brown clays seems to have IRM properties intermediate between the red sediments and the hydromorphous layer. The change in magnetic properties at 14 m most probably marks a change in hydrological conditions, affecting the magnetite component. The higher DP and lower SIRM for the magnetite component above 17 m are compatible with the effects of leaching of magnetite (van Oorschot *et al.* 2002). This could have occurred at any later time and might be related to the possible impermeability of the hydromorphous layer. However, this explanation remains speculative.

The spheroids of the haematite component for the interval of <14 m and the interval of >17 m run nearly parallel, suggesting that the process which formed/influenced the haematite above 17 m and below 14 m is similar. The haematite is probably formed *in situ*, as a result of weathering of silicates, giving rise to primary reddening (Turner 1980; Einsele 2000). The fact that the MT and the HT components display the same magnetic directions—without perceivable delay—indicates that the reddening occurred soon after deposition. Therefore, the HT component carries a primary NRM, as does the MT component.

5.3 A new cryptochron

We have reinterpreted the demagnetization data of Krijgsman *et al.* (1996), using the 360–570 °C temperature steps to represent the ChRM (Fig. 2). Krijgsman *et al.* (1996) had consistently used the 200–600 °C component in their original interpretation. Except when higher-temperature data were not available or of lower quality, they had chosen the 200–360 °C trajectory. However, we now know that it is important to select the same temperature steps for the ChRM—especially in these sediments—because of the LT overprint.

The largest difference between the two interpretations occurs in the interval from 0 to 5 m: the apparent short reversed-polarity zone within the uppermost part of the zone interpreted as C5n.1n appears to be an artefact of the LT component. Additionally, the interval containing the hydromorphous layer and limestone beds (15–30 m) does not give a clear polarity signal, because of weak magnetizations

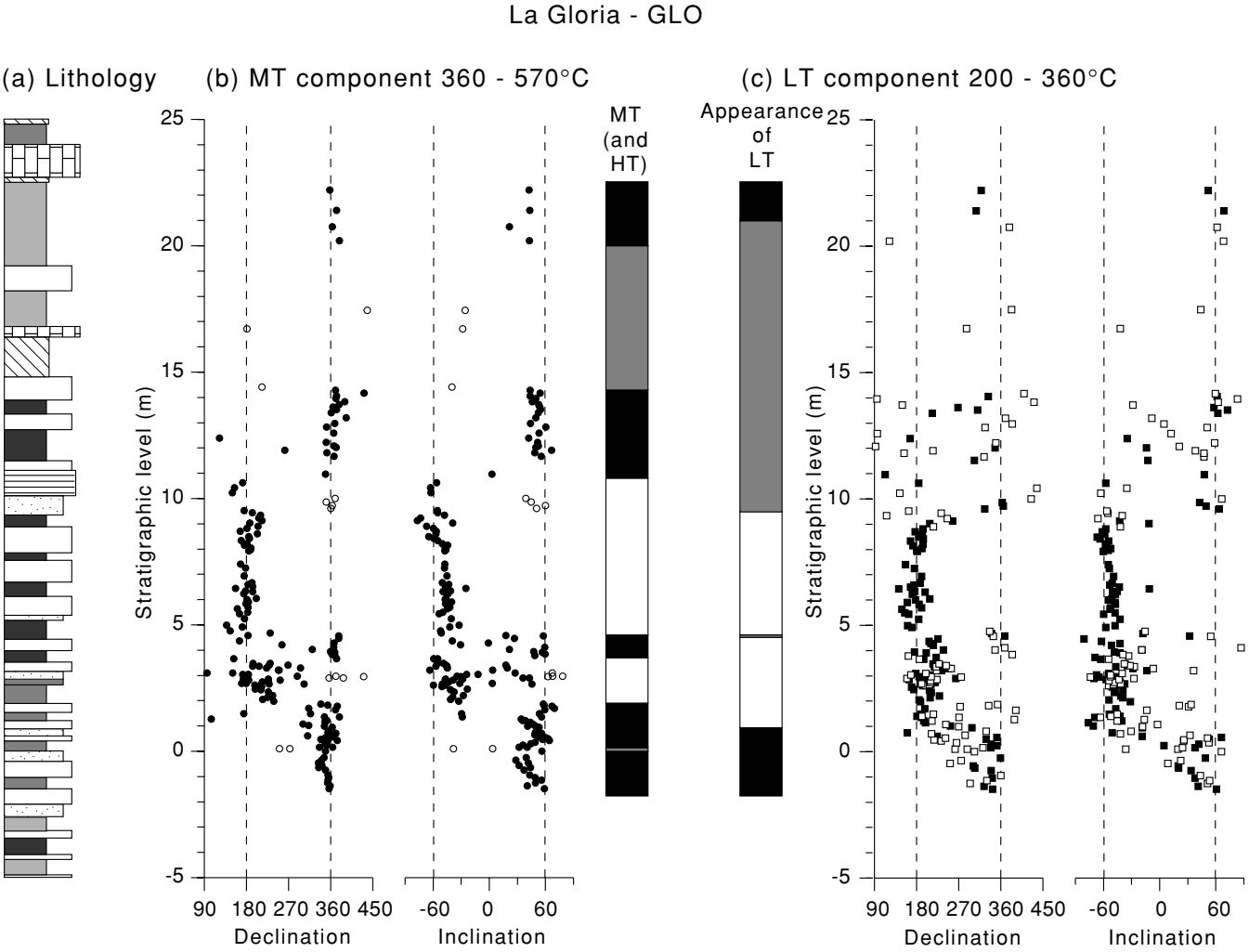

Figure 12. NRM directions of the resampled interval GLO versus stratigraphic level. (a) Lithological column, as in Fig. 2. (b) MT (360–570 °C) magnetostratigraphy (and HT 600–680 °C, not shown). Paleomagnetic directions that are regarded as less reliable are plotted as open circles. (c) LT (200–360 °C) 'magnetostratigraphy'. The LT component is interpreted as an overprint.

and low-quality demagnetization data. Therefore, the uppermost intervals are not interpreted in terms of polarity zones.

The magnetostratigraphy of the resampled section is shown in Fig. 12(b). Again, the magnetite component from 360 to 570 °C has been interpreted as the ChRM. The HT directions are not shown in Fig. 12(b), but give essentially the same directions as the MT component. Data from sandy layers are considered less reliable, because of their porous character, which makes them potential conduits for later groundwater percolation and remagnetization. Moreover, some deviating directions (∼2.9 and 9.6–10 m) are confined to the sandy layers, suggesting sedimentary artefacts rather than true geomagnetic directions. The hydromorphous layer (14.8–16.35 m, where goethite is dominant) and the brownish clays on top of it (16.35–18.2 m) did not give reliable results. The 'magnetostratigraphy' of the LT component, which is considered as a later reversed-polarity overprint, is given in Fig. 12(c). Although in some parts of the section the LT component appears to have normal polarity, this may be the result of the overlapping normal MT component. The original interpretation of Krijgsman *et al.* (1996) can be understood from the LT 'magnetostratigraphy'.

The general polarity partition of the detailed GLO series agrees with the lower-resolution GL series. However, instead of the reversed-polarity chron at stratigraphic level 2–11 m, we observe a normal polarity zone between two reversed-polarity intervals (2–3.7 and 4.6–11 m). Krijgsman *et al.* (1996) did not detect the normal polarity interval, probably because of their lower sampling resolution. An indication of the normal polarity interval in their record is apparent in one sample with an intermediate direction at ∼3.75 m, which was not assigned geomagnetic significance in the original study (Fig. 2). The IRM components do not indicate any unusual rock magnetic behaviour in the normal polarity interval, relative to the other parts of the section. Moreover, the normal polarity is not confined to one lithology only, but exists in both caliches and red clays. Therefore, the directions of the MT and HT components are considered reliable and thus the interval represents a normal polarity zone. If we assume that the basic cyclicity in the La Gloria section is linked to precession, then the durations of the reversed-polarity zone and the following normal polarity zone are approximately 21 kyr each. These durations explain why they are not present in the geomagnetic polarity timescale that is based on

marine magnetic anomalies. The maximum resolution in the marine magnetic anomaly pattern is approximately 30 kyr.

Although a new cryptochron has been detected, the more detailed sampling also revealed an ambiguous NRM signal in the section above 15 m. Moreover, when the long normal polarity zone in the lower part of the section represents C5n, the reversed Chron C5n.1r is missing in this section. This could either mean that there are hiati in the section or that the section is misplaced in the geomagnetic polarity timescale. Either way, the La Gloria section seems to be unsuitable for magnetostratigraphic purposes. Therefore, the La Gloria section should not be used to magnetostratigraphically date mammal biozones for biochronology.

6 CONCLUSIONS

Rock-magnetic analyses indicate that the magnetic remanence carriers in the red beds of La Gloria are magnetite and haematite. In the hydromorphous layer, goethite is dominant, whereas in the remainder of the section goethite is only present in minute quantities. From a magnetic point of view, the relative contributions of haematite and magnetite are approximately equal in the lower part of the section, while in the brown layers overlying the hydromorphous layer the relative contribution of magnetite is drastically reduced. This might be related to a change in the sedimentary environment, probably caused by a change in hydrological conditions.

The temperature-dependent behaviour of the NRM in the part of the section resampled at high resolution is characterized by up to four components: (1) a present-day field or laboratory overprint (<200 °C); (2) a low-temperature component (200–360 °C) is carried by part of the magnetite population. The LT component has a reversed polarity, and is regarded as an overprint; (3) a medium-temperature component (360–580 °C) is carried by part of the magnetite population. The MT component is interpreted as the ChRM; (4) a high-temperature component (600–680 °C) is carried by haematite. A simple model with a reversed LT and a normal MT component in various intensity ratios replicates the appearance of the NRM in demagnetization diagrams: zigzag or clusters of temperature steps in the range 200–360 °C. In the real data, the HT component shows no perceivable difference compared with the MT component, indicating that they both carry ChRM directions. Moreover, the behaviour of the NRM does not seem to be different between the red clay and the caliche layers.

The more detailed sampling reveals a new polarity zone, which probably represents a geomagnetic feature (i.e. cryptochron). However, the more detailed sampling also revealed ambiguous NRM signals in parts of the section. Consequently, the original magnetostratigraphy (Krijgsman *et al.* 1996) might not be reliable. We therefore dissuade the reader from using the La Gloria section as a dating tool for biochronological purposes.

ACKNOWLEDGMENTS

We thank Hayfaa Abdul Aziz and Frits Hilgen for their help in the field. We acknowledge Henk Meijer for measuring a substantial number of IRM curves. Discussions with Tom Mullender on the FORC analyses and his programming effort to interpret FORC diagrams are greatly appreciated. This work was funded by the Netherlands Organization for Scientific Research (NWO/ALW) and conducted under the programme of the Vening Meinesz Research School of Geodynamics (VMSG).

REFERENCES

Abdul Aziz, H., 2001. Astronomical forcing in continental sediments. An integrated stratigraphic study of Miocene deposits from the Calatayud-Teruel basin, NE Spain, *Geologica Ultraiectina,* **207,** 191 (*PhD thesis*, Utrecht University, Utrecht).

Abdul Aziz, H., Hilgen, F., Krijgsman, W., Sanz, E. & Calvo, J.P., 2000. Astronomical forcing of sedimentary cycles in the middle to late Miocene continental Calatayud Basin (NE Spain), *Earth planet. Sci. Lett.,* **177,** 9–22.

Baag, C.-G. & Helsley, C.E., 1974. Evidence for penecontemporaneous magnetization of the Moenkopi formation, *J. geophys. Res.,* **79,** 3308–3320.

Bloemendal, J., King, J.W., Hall, F.R. & Doh, S.-J., 1992. Rock magnetism of Late Neogene and Pleistocene deep-sea sediments: relationship to sediment source, diagenetic processes and sediment lithology, *J. geophys. Res.,* **97,** 4361–4375.

Calvo, J.P. *et al.*, 1993. Up-to-date Spanish continental Neogene synthesis and paleoclimatic interpretation, *Rev. Soc. Geol. España,* **6,** 29–40.

Calvo, J.P., Alonso-Zarza, A.M., van Dam, J. & Gutiérrez Santolalla, F., 1999. Estratigrafía y estructura del área de Los Mansuetos (Cuenca de Teruel). Precisiones papa la definición del estratotipo del Turoliense, *Geogaceta,* **25,** 55–58.

Channell, J.E.T., Freeman, R., Heller, F. & Lowrie, W., 1982. Timing of diagenetic haematite growth in red pelagic limestones from Gubbio (Italy), *Earth planet. Sci. Lett.,* **58,** 189–201.

Daams, R., van der Meulen, A.J., Alvarez Sierra, M.A., Pelaez-Campomanes, P. & Krijgsman, W., 1999. Aragonian stratigraphy reconsidered, and a re-evaluation of the middle Miocene mammal biochronology in Europe, *Earth planet. Sci. Lett.,* **165,** 287–294.

Dekkers, M.J., 1989. Magnetic properties of natural goethite-II. TRM behaviour during thermal and alternating field demagnetization and low-temperature treatment, *Geophys. J.,* **341,** 341–355.

Einsele, G., 2000. *Sedimentary Basins: Evolution, Facies, and Sediment Budget,* p. 792, Springer, Berlin.

Elston, D.P. & Purucker, M.E., 1979. Detrital magnetization in red beds of the Moenkopi formation (Triassic), Gray Mountain, Arizona, *J. geophys. Res.,* **84,** 1653–1665.

Hunt, C.P., Moskowitz, B.M. & Banerjee, S.K., 1995. Magnetic properties of rocks and minerals, *Rock Physics and Phase Relations, a Handbook of Physical Constants,* pp. 189–204, AGU Reference, American Geophysical Union, Washington DC.

Kirschvink, J.L., 1980. The least-squares line and plane and the analysis of palaeomagnetic data, *Geophys. J. R. astr. Soc.,* **62,** 699–718.

Krijgsman, W., Garcés, M., Langereis, C.G., Daams, R., van Dam, J., van der Meulen, A.J., Agustí, J. & Cabrera, L., 1996. A new chronology for the middle to late Miocene continental record in Spain, *Earth planet. Sci. Lett.,* **142,** 367–380.

Krijgsman, W., Delahaije, W., Langereis, C.G. & de Boer, P.L., 1997. Cyclicity and NRM acquisition in the Armantes section (Miocene, Spain): potential for an astronomical polarity time scale for the continental record, *Geophys. Res. Lett.,* **24,** 1027–1030.

Krijgsman, W., Delahaije, W., Langereis, C.G. & de Boer, P.L., 1999. Paleomagnetism and astronomically induced cyclicity of the Armantes section; a Miocene continental red bed sequence in the Calatayud–Daroca basin (Central Spain), *Acta Geol. Hisp.,* **32,** 201–219.

Kruiver, P.P. & Passier, H.F., 2001. Coercivity analysis of magnetic phases in sapropel S1 related to variations in redox conditions: what the *S*-ratio cannot explain, *Geochem. Geophys. Geosyst.,* **2,** 2001GC000181.

Kruiver, P.P., Dekkers, M.J. & Langereis, C.G., 2000. Secular variation in Permian red beds from Dôme de Barrot, SE France, *Earth planet. Sci. Lett.,* **179,** 205–217.

Kruiver, P.P., Dekkers, M.J. & Heslop, D., 2001. Quantification of magnetic coercivity components by the analysis of acquisition curves of isothermal remanent magnetisation, *Earth planet. Sci. Lett.,* **189,** 269–276.

Larson, E.E., Walker, T.R., Patterson, P.E., Hoblitt, R.P. & Rosenbaum, J.G., 1982. Paleomagnetism of the Moenkopi formation, Colorado Plateau:

basis for long-term model of acquisition of chemical remanent magnetism in red beds, *J. geophys. Res.,* **87,** 1081–1106.

Molina-Garza, R.S., Geissman, J.W., van de Voo, R., Lucas, S.G. & Hayden, S.N., 1991. Paleomagnetism of the Moenkopi and Chinle formations in central New Mexico: implications for the North American apparent polar wander path and Triassic magnetostratigraphy, *J. geophys. Res.,* **96,** 14 239–14 262.

Mullender, T.A.T., van Velzen, A.J. & Dekkers, M.J., 1993. Continuous drift correction and separate identification of ferrimagnetic and paramagnetic contributions in thermomagnetic runs, *Geophys. J. Int.,* **114,** 663–672.

Néel, L., 1955. Some theoretical aspects of rock magnetism, *Adv. Phys.,* **4,** 191–242.

Pike, C.R., Roberts, A.P. & Verosub, K.L., 1999. Characterizing interactions in fine magnetic particle systems using first order reversal curves, *J. Appl. Phys.,* **85,** 6660–6667.

Pike, C.R., Roberts, A.P., Dekkers, M.J. & Verosub, K.L., 2001. An investigation of multi-domain hysteresis mechanisms using FORC diagrams., *Phys. Earth planet. Inter.,* **126,** 13–28.

Roberts, A.P., Cui, Y. & Verosub, K.L., 1995. Wasp-waisted hysteresis loops: mineral magnetic charecteristics and discrimination of components in mixed magnetic systems, *J. geophys. Res.,* **100,** 17 909–17 924.

Roberts, A.P., Pike, C.R. & Verosub, K.L., 2000. First-order reversal curve diagrams: a new tool for characterising the magnetic properties of natural samples, *J. geophys. Res*., **105,** 28 461–28 475.

Steiner, M.B., 1983. Detrital remanent magnetization in haematite, *J. geophys. Res.,* **88,** 6523–6539.

Tauxe, L. & Badgley, C., 1984. Transition stratigraphy and the problem of remanence lock-in times in the Siwalik red beds, *Geophys. Res. Lett.,* **11,** 611–613.

Tauxe, L., Kent, D.V. & Opdyke, N.D., 1980. Magnetic components contributing to the NRM of middle Siwalik red beds, *Earth planet. Sci. Lett.,* **47,** 279–284.

Tauxe, L., Mullender, T.A.T. & Pick, T., 1996. Potbellies, wasp-waists, and superparamagnetism in magnetic hysteresis, *J. geophys. Res.,* **101,** 571–583.

Turner, P., 1980. *Continental red beds*. Vol. 29, *Developments in Sedimentology,* p. 562, Elsevier, Amsterdam.

van Dam, J., Alcalá, L., Alonso Zarza, A., Calvo, J.P., Garcés, M. & Krijgsman, W., 2001. The Upper Miocene mammal record from the Teruel–Alfambra region (Spain). The MN system and continental stage/age concepts discussed, *J. Vert. Paleontol.,* **21,** 367–385.

van der Meulen, A.J. & Daams, R., 1992. Evolution of Early-Middle Miocene rodent faunas in relation to long-term palaeoenvironmental changes., *Palaeogeog. Palaeoclimat. Palaeoecol.,* **93,** 227–253.

van Hoof, A.A.M., van Os, B.J.H., Rademakers, J.G., Langereis, C.G. & de Lange, G.J., 1993. A paleomagnetic and geochemical record of the Upper Cochiti reversal and two subsequent precessional cyles from Southern Sicily., *Earth planet. Sci. Lett.,* **117,** 235–250.

van Oorschot, I.H.M., Grygar, T. & Dekkers, M.J., 2001. Selective dissolution of magnetic iron oxides in the acid-ammonium-oxalate/ferrous-iron extraction method – I. Synthetic samples, *Geophys. J. Int.,* **145,** 740–748.

van Oorschot, I.H.M., Dekkers, M.J. & Havlicek, P., 2002. Selective dissolution of magnetic iron oxides with the acid-ammonium-oxalate/ferrous-iron extraction technique – II. Natural loess and palaeosol samples, *Geophys. J. Int.,* **149,** 106–117.

Walker, T.R., Larson, E.E. & Hoblitt, R.P., 1981. Nature and origin of haematite in the Moenkopi Formation (Triassic), Colorado Plateau: a contribution to the origin of magnetism in red beds, *J. geophys. Res.,* **86,** 317–333.